Optical Engineering

OpticalEngineering.SPIEDigitalLibrary.org

Double-meander spring silicon piezoresistive sensors as microforce calibration standards

Gerry Hamdana
Hutomo Suryo Wasisto
Lutz Doering
Chunlei Yan
Lei Zhou
Uwe Brand
Erwin Peiner

SPIE.

Gerry Hamdana, Hutomo Suryo Wasisto, Lutz Doering, Chunlei Yan, Lei Zhou, Uwe Brand, Erwin Peiner, "Double-meander spring silicon piezoresistive sensors as microforce calibration standards," *Opt. Eng.* **55**(9), 091409 (2016), doi: 10.1117/1.OE.55.9.091409.

Double-meander spring silicon piezoresistive sensors as microforce calibration standards

Gerry Hamdana,[a,b,*] Hutomo Suryo Wasisto,[a,b] Lutz Doering,[c] Chunlei Yan,[a] Lei Zhou,[a] Uwe Brand,[c] and Erwin Peiner[a,b]
[a]Technische Universität Braunschweig, Institute of Semiconductor Technology (IHT), Hans-Sommer-Straße 66, D-38106 Braunschweig, Germany
[b]Laboratory for Emerging Nanometrology (LENA), Hans-Sommer-Straße 66, D-38106 Braunschweig, Germany
[c]Physikalisch-Technische Bundesanstalt (PTB), Department 5.1 Surface Metrology, Bundesallee 100, D-38116 Braunschweig, Germany

Abstract. A transferable force calibration standard based on a silicon microelectromechanical sensor has been designed, fabricated, and characterized for micrometrology applications. Two essential elements of double-meander springs and full piezoresistive etched *p*-silicon-on-insulator Wheatstone bridges (WBs) are integrated to the sensor for enhancing the device's sensitivity and eliminating the current leakage during an active sensing operation, respectively. The design process is supported by three-dimensional finite element modeling to select the optimal proposed sensors as well as simulating their mechanical and electrical properties in the desired force range ($\leq$1000 μN). To fabricate the microforce sensors, a bulk micromachining technology is used by frequently involving an inductively coupled plasma deep reactive ion etching at cryogenic temperature. Several optical and electrical characterization techniques have been utilized to ensure the quality of the fabricated WBs, where their measured offset voltage can be down to 0.03 ± 0.071 mV/V. In terms of its linearity, the fabricated device exhibits a small nonlinearity of <3%, which leads this sensor to be appropriate for precise microforce standard. [DOI: 10.1117/1.OE.55.9.091409]

Keywords: calibration standard; double-meander springs; dry etching; force sensor; force calibration; stiffness.

Paper 160102SS received Jan. 20, 2016; accepted for publication Apr. 28, 2016; published online May 27, 2016.

1 Introduction

Trends toward miniaturization require not only suitable fabrication technology of the systems at microscale, but also reliable measurement techniques for its physical properties. In this context, measurement systems are expected to provide more precise values in smaller unit. Force—as one of the most important physical parameters—plays an enormous role in technological advances of humankind, both in fundamental research and applications. Moreover, to determine small force precisely, appropriate sensors are needed.

To date, several sensing mechanisms of sensors have been developed in recognizing small forces (e.g., changes of magnetic flux, capacitive, and piezoresistive). Mehrtash et al.[1] developed a system utilizing a magnetic field to determine the environmental forces in the microdevice for human drug delivery. Meanwhile, polydimethylsiloxane-based force sensors also have been introduced utilizing the overlap between two electrodes on their top and bottom sides, which can detect forces in normal and tangential directions through the change of capacitance values.[2] Hence, those flexible sensors were targeted for natural sensing mechanism with capability to measure weight and deflection of <10 mg and 8 μm, respectively. Nevertheless, transducing a mechanical into electrical signal by using the piezoresistive effect is still dominant in many sensing applications. Utilizing this effect, pressure sensors were fabricated and tested to determine sensitivity and linearity of different piezoresistive configurations at different temperatures.[3] In this context, sensor design made of parallel transverse resistors has better sensitivity and linearity than a single transverse resistor. In contrast, two longitudinal strain gauges were integrated into a cantilever-based microforce sensor.[4] The stress was applied on the free end of the beam structure with a length of 700 μm, a width of 20 μm, and a thickness of 12 μm, which could be used for measuring forces on a microgripper. After calibration, this type of sensor demonstrated stiffness and sensitivity of $\sim$130 N/m and $\sim$5063 V/N, respectively. Despite excellent sensitivity, the sensor was still too rigid, especially for applications in the fields of precision engineering (e.g., hardness measurement instruments, medical instruments, and micro-macro bilateral control).

Furthermore, another application of use for a microforce sensor is the nanoindentation, which is basically a technique allowing mechanical characterization of materials by applying defined load or deflection onto the sample, so that its hardness can be determined.[5] With the aim of broader force range and applications, depth sensing instruments have been successfully developed in the past to obtain a resolution of 1 nN and a displacement of <1 nm. However, to ensure the highest quality of indentation instruments, reliable calibration procedures are still required, especially for lower force range application (i.e., systems with haptic force-feedback in minimal invasive surgery).[6] Han et al.[7] developed piezoresistive ring-shaped axial sensors to predict forces during catheterization. This sensor was attached on the tip on the guidewire and its movements in z-direction led to deformation of the ring structure as well as the piezoresistive elements. Their thin resistors were fabricated on silicon-on-insulator (SOI) wafer, which showed a sensitivity value of $\sim 13.4 \times 10^{-3}$ μm^{-1} in z-direction.

*Address all correspondence to: Gerry Hamdana, E-mail: g.hamdana@tu-bs.de

In addition to this, precise measurement of small forces is also useful for applications in robotics (e.g., macro-micro-bilateral control). Transfers of real-world haptic information (i.e., force and position) from microenvironment (target object) into the macrosurrounding (operator) are important for further development of medical technology.[8] However, to realize this kind of operation control, the disturbances have to be taken into account. Mizutani and Katsura[9] compensated the disturbances of the control system by integrating the saving and loading system within closed-loop operation. Furthermore, since the disturbances were also usually scaled, scaling rate is very important to determine whether the effect of the disturbances within a system can be neglected or not. Therefore, precise measurements of environmental reactions are needed to obtain the highest possible transparency, which can only be performed by compensating the disturbances.[10,11]

In this work, we proposed a stable microforce sensor based on double-layer (DL) SOI as transferable calibration standards. Unlike the similar calibration standard, our sensor was mainly fabricated employing an inductively coupled plasma (ICP) deep reactive ion etching (DRIE) process at cryogenic temperature.[12] Therefore, anisotropy of the process can be controlled and integration of meander structures into the device is feasible. On both clamped ends, two piezoresistive strain gauges are used as active sensing elements. Therefore, the sensors have direct force-reading capability. To evaluate their performances, static and dynamic properties of the devices were characterized showing promising results to broaden their industrial applications (e.g., mechanical feedback control and robotics).

2 Sensor Design and Simulation

2.1 *Finite Element Modeling*

In this initial effort, three different designs of SOI-based double-meander spring sensors were modeled, and an extensive micromechanical finite element modeling (FEM) was performed using COMSOL Multiphysics 4.3b.[13] However, the interest of this study was to determine the impact of different design configurations to sensor characteristics (i.e., stiffness, linearity, and sensitivity). Considering the real sensor geometry, a three-dimensional (3-D) model was constructed instead of a simplified two-dimensional model. In general, the sensor consists of three main components: contact area in the center (boss), double spring structures flanking to the boss, and piezoresistive Wheatstone bridges (WBs) clamped on both ends of the chip [Figs. 1(a)–1(c)]. While the sensor spring was varied into three designs, the main area of the device was kept to be identical (i.e., 20 mm × 2.2 mm). Several different mesh sizes were manually chosen for different 3-D structures to save computational time without compromising any reliability of the simulation results.[14] Moreover, single crystal anisotropic p-doped silicon was chosen from the COMSOL library. The models were either rotated 45 deg in the xy-plane or a rotated coordinate system was defined using z–x–z convention of Euler angle to perform simulation along ⟨110⟩ crystal orientation.[13,15,16] Therefore, comparable physical properties with a fabricated sensor can be determined.

Meanwhile, mechanical and electrical properties of the devices were computed with two physics interfaces from the MEMS module, i.e., solid mechanics (solid) and piezoresistivity, domain currents (pzrd). All exterior mechanical boundaries of the sensor spring were set to be free, excluding the bottom part of the sensor frame, which was set to be fixed during force loading on the center part of the boss. For the electrical boundaries, an electrical potential of 1 V was applied to one of the electrode contacts from the WB as a dc input voltage (V_{in}). Meanwhile, another contact electrode, which is diagonally aligned to the input electrode, was grounded. Thus, the offset voltages could be read from the other two diagonal nodes of the WB (V_{off}).

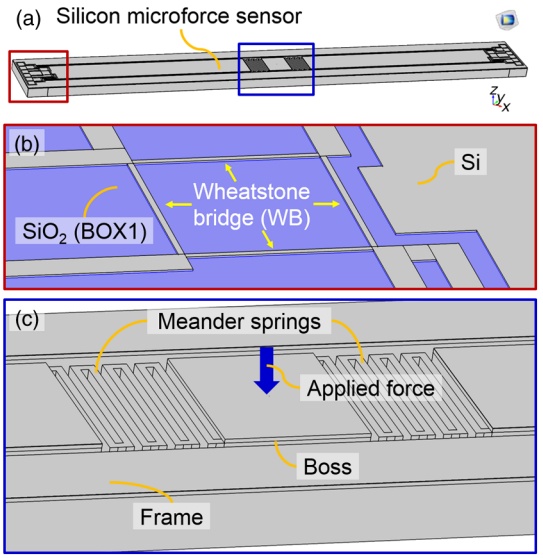

Fig. 1 3-D finite element model of (a) the proposed silicon microforce sensor comprising (b) two identical etched WBs located close to the clamped ends and (c) the double-meander springs flanking to the boss.

Three different sensor designs were differentiated by the shape of the spring structure close to the boss, although their total dimensions were kept equal (i.e., 750 μm in length and 1000 μm in width). Perpendicular to xy-plane, design 1 has deep and small gap meander structures [Fig. 2(a)]. Compared to this, the spring design 2 has meander structures upright to the xy-plane or vertically aligned, which will require a more complex fabrication process to create such a rectangular corrugated surface profile [Fig. 2(b)]. On the other hand, the spring design 3 uses only simple thin membranes instead of meander structures as its spring component [Fig. 2(c)].

2.2 *Simulation Results on Device Stiffness and Sensitivity*

The numerical search of the optimal geometry configuration of the sensors is based on both mechanical and electrical properties (i.e., stiffness, nonlinearity, and sensitivity). The device models were assessed within the targeted application force range (i.e., between 0 and 1000 μN with a force increment of 100 μN). Deflection states of three different sensor designs under a force up to 1000 μN are shown in Fig. 4(a). Based on the assumption that the sensor elastically deforms and the origin of the coordinate system (x, y, and z) is located on the clamping area of the neutral layer [Figs. 3(a)–3(b)], a point load F applied on the boss structure induces a bending moment M_b, which results in tensile stress σ_L in ⟨110⟩

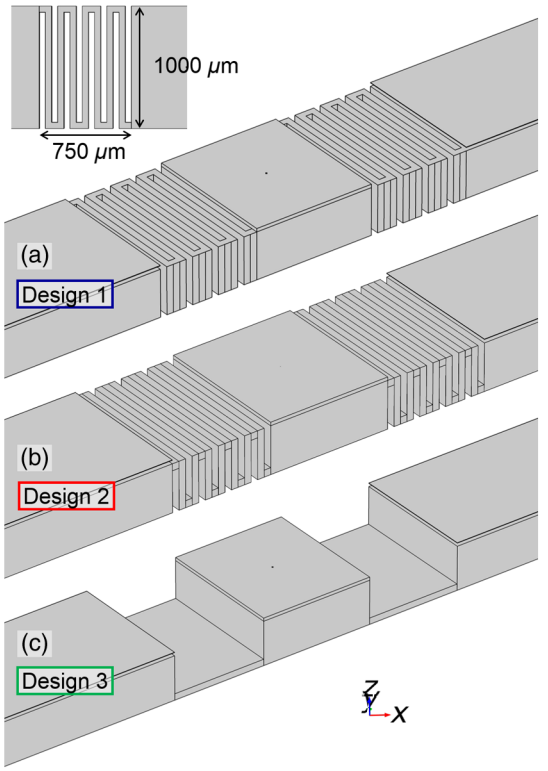

Fig. 2 Three spring modifications of the enhanced microforce sensors showing (a) design 1 with horizontal meander structures on a flat surface profile, (b) design 2 with vertical meander structures on a rectangular corrugated surface profile, and (c) design 3 with flat rectangular plates fixed on the bottom of the boss.

directions. The stress is distributed along the rectangular beam, which can be given as

$$\sigma_L = \frac{12(l-x)z}{wt^3}F, \tag{1}$$

where z, x, l, w, and t are the distance from the neutral layer along the z-axis, a certain position on the x-axis, length, width, and thickness of the beam, respectively.[17] In this case, WB structures are placed on the location where the highest mechanical stress $\sigma_{L,\max}$ is to be expected to occur, i.e., as far as possible from the applied force (x value should be minimum) and on the surface of the beam (z value should be $t/2$). Depending on Young's modulus E, the elongation ε_L may be expressed as

$$\varepsilon_L = \frac{\sigma_L}{E}. \tag{2}$$

Considering the same deflection value, the stress can be quantified through the bending radius r, which defines later the deformation of the WB structures and is accordingly determined as

$$r = \frac{z}{\varepsilon_L}. \tag{3}$$

The force needed to obtain the same deflection value depends on the material, geometry, and bending properties, which is defined as

$$F = \frac{wt^3E}{12r(l-x)}, \tag{4}$$

and the stiffness k is defined by the ratio of the applied force to the outcome deflection.

$$k = \frac{\Delta F}{z}, \tag{5}$$

where ΔF and Δz are the applied load and boss deflection increments, respectively. Among the selected approaches, design 1 was evaluated to have the most compliant structure with a stiffness of $23.39 \pm 9 \times 10^{-9}$ N/m, which is around 4.5 times smaller than that of design 2 (i.e., $103.45 \pm 1.6 \times 10^{-12}$ N/m). As expected for a membrane spring, the structure of design 3 has resulted in the highest stiffness value of $6236.86 \pm 2 \times 10^{-9}$ N/m [Fig. 4(b)]. In this case, the higher stiffness value indicates a more rigid behavior of the spring structure. Therefore, it can lead to better linearity of the force-deflection curves.

Apart from the stiffness and linearity, another essential quality characteristic of the device is sensor sensitivity. Because the output signal of the device is read using a piezoresistive method, the sensitivity in this circumstance is related to the WB performance. As a result, the sensitivity of a microforce sensor is defined to be the change in the WB resistance values ($\Delta R/R$), which depends on the change of mechanical stress on the surface and the piezoresistive coefficient in longitudinal (σ_L, Π_L) and transverse directions (σ_T, Π_T).

$$\frac{\Delta R}{R} = \sigma_L \Pi_L + \sigma_T \Pi_T. \tag{6}$$

In the simulation, these piezoresistive effects are directly represented as output voltages with regard to the change in the applied force.[18] Moreover, doping concentrations on the WB and its electrical contact extensions are set to be 5×10^{18} cm^{-3} and 1×10^{19} cm^{-3}, respectively. Afterward, a supply voltage (V_{in}) of 1 V and the ground were applied through the diagonal opposite pads. Hence, the change of the output voltage (V_{off}) on the WB by different force loads can be measured, which is given as

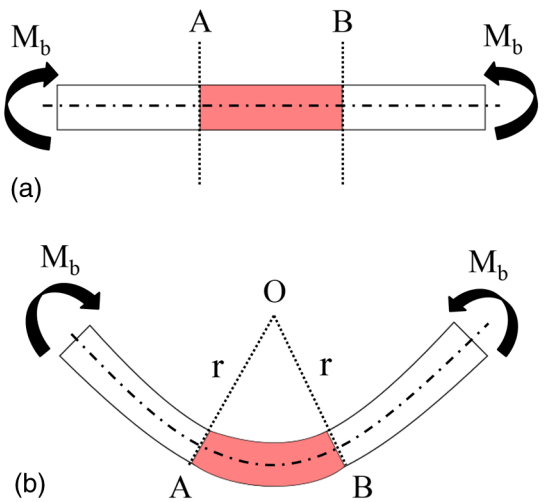

Fig. 3 Bending mechanism of microforce sensor: (a) before and (b) after beam deformation.

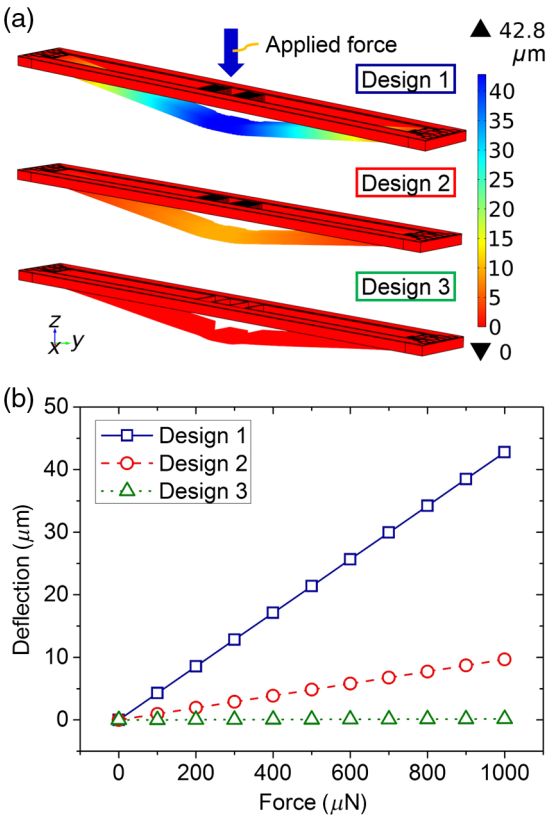

Fig. 4 (a) 3-D FEM results showing the conditions of three different designed microforce sensors under a force loading up to 1000 μN. The color legend describes the device displacement in micrometer scale. (b) Maximum displacements of their boss structure as a function of applied vertical force on its center position. Design 1 exhibits the most compliant structure among them.

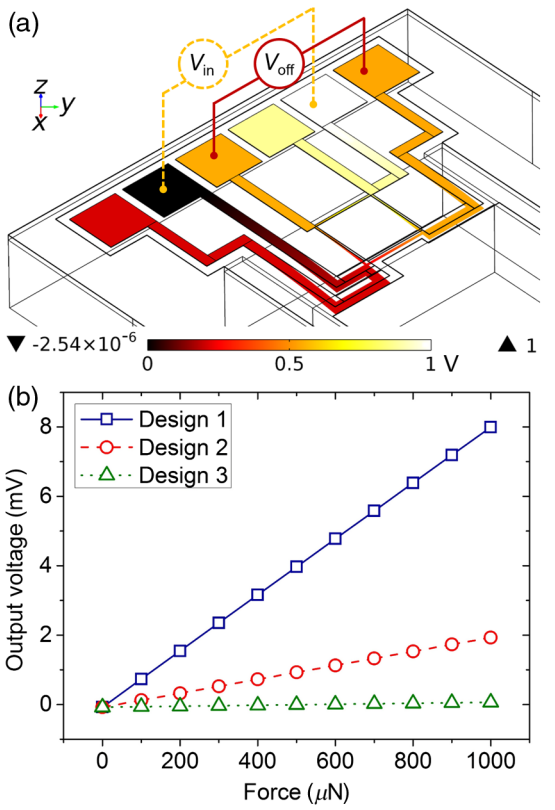

Fig. 5 (a) 3-D FEM results demonstrating the etched silicon piezoresistors designed in a full WB circuit under a force loading up to 1000 μN. The color legend describes the voltage distributed on the device structure in V-unit. (b) Sensor sensitivity of the sensors as a function of applied vertical force on its center position.

$$V_{\text{off}} = V_{\text{in}} \times \left(\frac{R_2}{R_1 + R_2} + \frac{R_3}{R_3 + R_4} \right), \tag{7}$$

where R_1, R_2, R_3, and R_4 are given resistor values corresponding to a full WB configuration. In Fig. 5(a), the distribution of voltage in the WB circuit under applied forces up to 1000 μN is presented. The sensitivity (S) is then calculated through the output voltage values (ΔV_{out}) of different sensor architectures by different force loads ($\Delta F = 0$ to 1000 μN) with an increment of 100 μN, which can be defined as

$$S = \frac{\Delta V_{\text{out}}}{F}. \tag{8}$$

It is found that design 1 has the highest electromechanical sensitivity of 8.07 ± 0.004 V/N, which is much higher than those of design 2 (i.e., $2.01 \pm 3 \times 10^{-4}$ V/N) and design 3 (i.e., $0.14 \pm 8 \times 10^{-7}$ V/N) by a factor of ~4 and ~57, correspondingly [Fig. 5(b)]. Thus, design 1 can provide high sensor output voltages at relatively low applied forces. A comparison of the performed FEM of different sensor designs is shown in Table 1. These results suggest that design 1 with horizontal meander structures is superior to the other designs in terms of both stiffness and sensitivity with only relatively small standard deviation (<1%). Therefore, design 1 has been chosen for the device fabrication.

3 Sensor Fabrication

3.1 *Fabrication Process Steps*

After engineering the designs and analyzing the simulation results, microforce sensors were fabricated to match the geometry of design 1. For this purpose, commercial p-type DL-SOI

Table 1 Simulation results of the microforce sensors with three different spring designs observed in the force range of 0 to 1000 μN.

Data	Microforce sensor		
	Design 1	Design 2	Design 3
Spring type	Horizontal meander structure with a flat surface profile	Vertical meander structure with a rectangular corrugated surface profile	Flat rectangular plate fixed on the bottom of the boss
Stiffness (N/m)	23.39 $\pm 9 \times 10^{-9}$	103.45 $\pm 1.6 \times 10^{-12}$	6236.86 $\pm 2 \times 10^{-9}$
Nonlinearity (%)	$\ll 1$	$\lll 1$	$\lll 1$
Sensitivity (V/N)	8.07 ± 0.004	$2.01 \pm 3 \times 10^{-4}$	$0.14 \pm 8 \times 10^{-7}$

Table 2 Material specification of the DL-SOI used for meander spring microforce sensors.

Specification	Data
Wafer type	DL-SOI
Resistivity	0.01 to 0.02 Ωcm
Type/dopant	*p*-type/boron
Thickness	Device layer = (3 ± 1) μm
	BOX1 = (0.2 ± 0.01) μm
	Middle layer = (25 ± 0.5) μm
	BOX2 = (0.5 ± 0.025) μm
	Handle layer = (350 ± 15) μm

wafers with ⟨100⟩ orientation and a resistivity of the top layer of 0.01 to 0.02 Ωcm were used (Active Business Company GmbH, Germany). According to the manufacturer, the device, middle, and handle layers have thicknesses of (3 ± 1) μm, (25 ± 0.5) μm, and (350 ± 15) μm, respectively. Between those silicon layers, two isolation layers of buried oxides (i.e., BOX1 and BOX2), which are located on the upper and lower positions, possess thicknesses of (0.2 ± 0.01) μm and (0.5 ± 0.025) μm, respectively. The physical parameters of the wafer are summarized in Table 2.

Sensor fabrication was conducted based on silicon bulk micromachining processes. The key fabrication steps are schematically shown in Fig. 6, which can be described in detail as follows:

1. Sensor fabrication started with cutting a 4-in. DL-SOI wafer into pieces with dimensions of 26 mm × 26 mm. After being diced, the sample was treated in a piranha cleaning (i.e., $H_2O_2 : H_2SO_4 = 1:1$) inside a quartz glass, which was subsequently boiled on a hot plate with a temperature of 90°C for 5 min to remove any organic residues on the sample during fabrication (e.g., before and after thermal oxidation and prior to photolithography).
2. To achieve higher quality contact formation to the etched *p*-WB, p^+-diffusion (boron) was applied on the device layer under a temperature of 1200°C within 30 min. Prior to this step, combination of dry and wet oxidation processes at 1100°C was used to create ∼300-nm-thick SiO_2.
3. 3-μm-thick WB structures were created on the device layer using DRIE at cryogenic temperature (Sentech Instruments GmbH). A 1.7-μm-thick S1818 photoresist was used as an etching mask and two etch gases (i.e., O_2 and SF_6) were employed. Finally, a recipe of ICP source power of 500 W, a high-frequency power of 6 W, a process temperature of −80°C, an SF_6 flow of 129 sccm, and an O_2 gas flow of 7 sccm was used.
4. The oxide layer on the middle of the device (BOX1) was structured using buffered hydrofluoric acid (HF, 6 to 7%). Afterward, metal films (30/300-nm-thick Cr/Au) were applied on the top of the device using e-beam evaporator. Lift-off process was then utilized to define the location of the metal layer. During this process, the metal marking in the middle of the boss structure was also created as a reference for the defined positioning of the stylus on the boss.
5. In the next step, photolithography and DRIE were performed for both the top and front sides of the device. By employing photoresist as an etching mask, the boss structure and the front side of the spring were defined. In this case, the 25-μm-thick silicon middle layer was etched with the same recipe as the WB structures within 12 to ∼15 min. Subsequently, the second buried oxide layer (BOX2) was removed by dipping the sample into buffered HF (6 to 7%).
6. The most challenging step during the device fabrication was the etching step of the meander structure from the backside of the device. A recipe with an ICP source power of 500 W, a high-frequency power of 7 W, a temperature of −75°C, and gas flow of 129 sccm (SF_6) and 6 sccm (O_2) was used for this etch process step to release the deep structure (300 μm) with small gaps (50 μm). Due to nonuniform temperature distribution during the etching process, parts of structures were overetched. Therefore, in terms of a fixed recipe, etch duration should be adjusted carefully (i.e., ∼1.5 h).

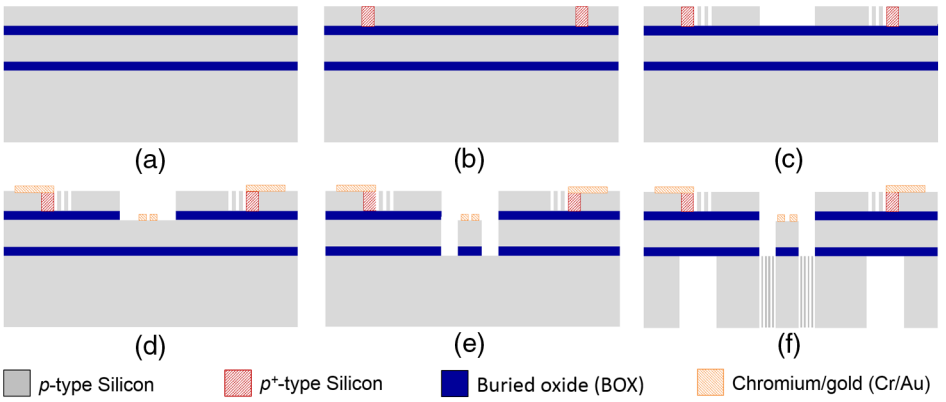

Fig. 6 Schematics of the process flow for the fabrication of the double-meander spring microforce sensors, including (a) wafer preparation, (b) boron diffusion with a thermal oxide mask, (c) WB etching, (d) metallization, (e) topside spring dry etching, and (f) backside meander spring release.

3.2 *Fabricated Active Microforce Sensors*

After being released from the fabrication batch, the 26 mm × 26 mm large samples were then diced into six single piezoresistive-based microforce sensing devices [i.e., each sensor has a dimension of 20 mm × 2.2 mm, see Fig. 7(a)] by taking the advantage of an annexed thin membrane located to one of the sensor frame sides. Thus, in this case, a tweezer can be used instead of a more complicated and expensive dicing blade tool to separate the sensors from the dies. The sensors were then taken to be examined optically in a scanning electron microscope (SEM). On both ends of the front side, WBs as active sensing elements were created to characterize mechanical tension during material deformation [Fig. 7(b)]. These locations close to clamped ends are expected to have the maximum stress levels along the sensor beam length, which have been proven from FEM (i.e., ~3 to 7×10^7 N/m^2 for an applied force of 1 mN). The conversion of the material deformation into an electrical signal was carried out by the implemented piezoresistive mechanism. Moreover, the design of full *p*-type WBs may have better performance with regard to temperature effect cancellation compared to a half-bridge circuit. Meanwhile, for their vertical thickness, the fabricated resistors exhibit very high uniformity attributed to the predefined SOI-material thickness. This would be beneficial compared to the conventional diffused or implanted *p*-type resistors on *n*-type substrates for better designing and controlling the precise resistance values of the piezoresistors (i.e., in the range of kΩ).[19,20] Therefore, we could obtain well-defined perpendicularly arranged resistors [Fig. 7(c)]. However, it should also be noted that the oxide areas surrounding the bridge had been extended compared to the former design (i.e., 40 μm) to avoid unwanted micro/nanoparticles shorting the active silicon regions.[21] This phenomenon could either occur during wire bonding or sensor characterization.

In addition to the WB structures, we also characterized the fabricated spring structures on the device optically. Figure 8(a) shows the boss and both clamped meander spring structures viewed from the bottom side. Although there were some imperfections of the overetched areas on the structures, which might be caused by nonuniform temperature distribution during the etch process, these meander structures were still expected to be able to improve the sensor performance [Fig. 8(b)]. Another possible reason for this case was the used self-bias set by the high-frequency power. Nevertheless, this type of artifact could be reduced or

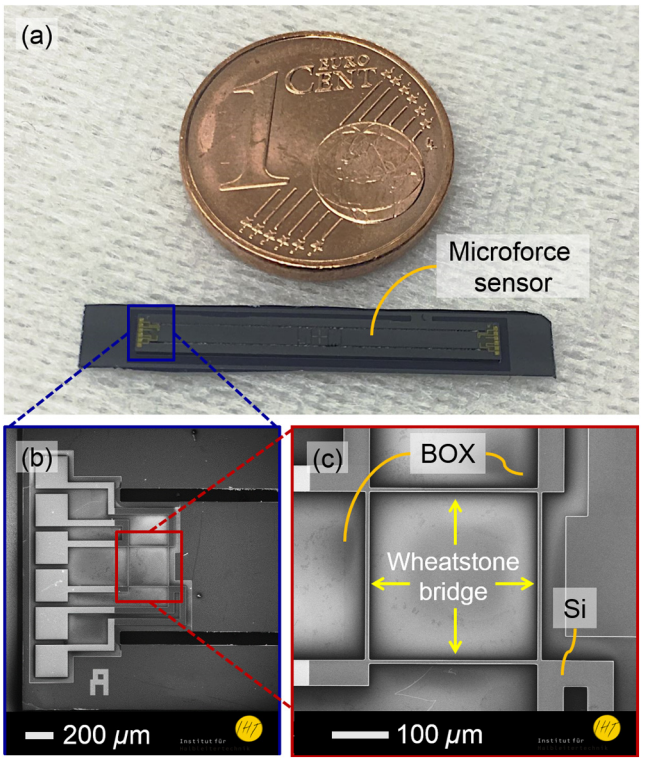

Fig. 7 (a) Optical and (b) scanning electron microphotographs of the fabricated active silicon microforce sensors showing (c) the etched piezoresistive WB structures at the sensor clamped end.

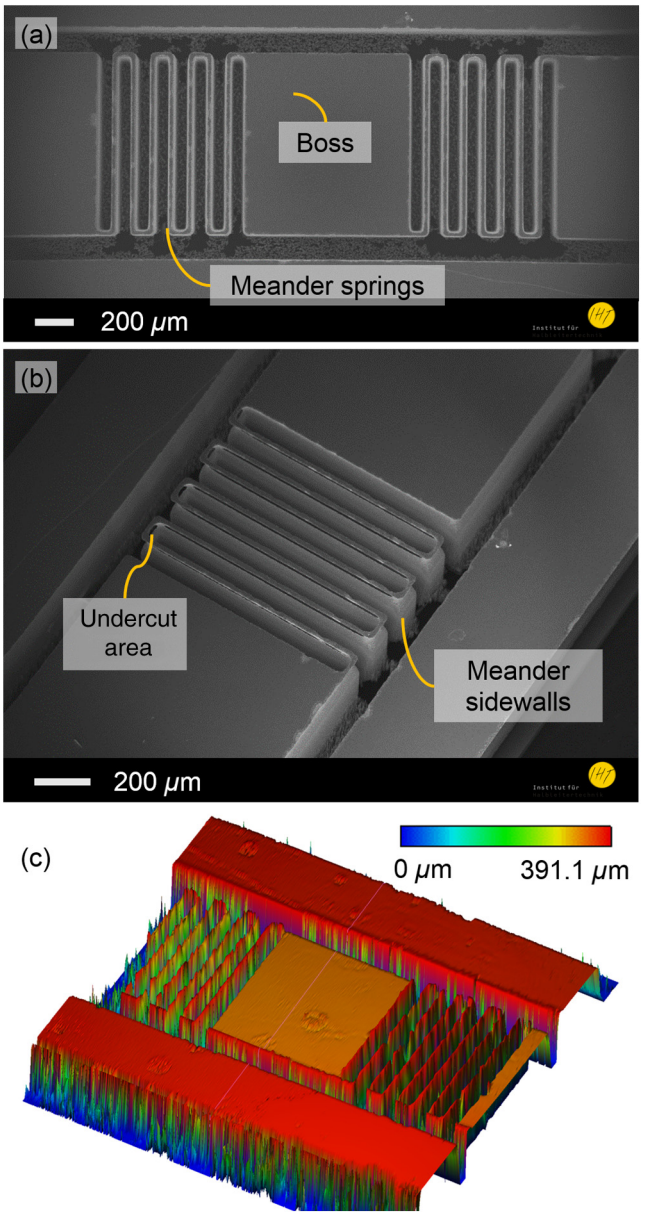

Fig. 8 SEM images of (a) the middle part of the active microforce sensor showing its meander springs flanking over the boss structure. (b) Some undercut areas on the meander structures viewed from the bottom side. (c) 3-D surface profile of meander springs measured with 3-D laser microscopy.

even eliminated by better adjustment of the etch recipe. Hence, smoother trench sidewalls as well as more uniform silicon blocks could be obtained.[21,22] Furthermore, a 3-D laser microscope (LEXT OLS4000 3D Laser Measuring Microscope, OLYMPUS) was used to measure the meander actual geometry and its surface profile after fabrication. It can be obviously seen from the extracted 3-D micrograph [Fig. 8(c)] that although the meander structures show good uniformity and perpendicular walls on their structure, their actual size has been shrunk to be smaller than designed and modeled geometry (i.e., from 50 to 35 μm), which may affect the performance of the sensors, especially for their stiffness.

3.3 *Piezoresistive Wheatstone Bridges*

The dimensions (i.e., width and thickness) of the fabricated WB structures are measured using SEM and a 3-D laser microscope. The full image of the WB and its magnification of several critical positions were captured and analyzed (s. Fig. 9). The measured width single resistor geometry exhibits very low deviation (~1.3%) for the investigated WBs with an average value of 7.20 ± 0.10 μm. As a consequence, the offset voltage of the fabricated WBs was also low (i.e., expected to be $V_{\text{off}} < 10$ mV/V). Ideally, the offset voltage should be zero. However, due to imperfections of fabrication processing steps, such small values in practical situations can still be acceptable for signal processing of the piezoresistive sensors.

Moreover, two neighboring WB structures, which are located next to each other at 90 deg angle, were measured by a 3-D laser microscope [Figs. 10(a)–10(c)]. The functional structure under line A is by 0.20 μm narrower than that under line B. In addition, the structure under line A has a height of ~2.8 μm compared with the structure under line B of 2.7 μm, which are within the manufacturing tolerance of the DL-SOI device layer (i.e., 3 ± 1 μm). It should be noted that the measurements were also performed for the other three corners of the WB, which yielded similar results as the described one. These values demonstrate that the geometry deviation during the etching was relatively small with maximum values of 0.1 and 0.2 μm in vertical and horizontal directions, respectively. Therefore, the etch recipe can be used to reproducibly fabricate etched WBs with structure dimensions matching that of the employed lithography mask.

In this work, two different metallization forms were applied on the devices (i.e., full- and half-metal contacts). The full metal type covers the whole electrical path surfaces from the contact pads to the WB corners [Fig. 11(a)]. For the half-metal contact, the Cr/Au layer was deposited only on the top of a defined area outside the membrane [Fig. 11(b)]. This second metallization design was made considering the avoidance of an additional stress from full metal on the thin membrane area where the WB was located. However, the implementation of different metallization designs has consequences on the wire resistance values, which can be determined from the measured resistance values between contacts 2 and 3 as well as 5 and 6, i.e., R_{23} and R_{56}. In Table 3, the measured resistances $R_{13}, R_{14}, R_{16}, R_{34}, R_{36}$, and R_{46} are listed. As expected, higher values were observed with half-metal stripes owing to the higher wire resistance. However, the offset values of both options, which were reasonably low in both cases (i.e., <10 mV/V), showed much lower values for the half-metal stripes (0.03 ± 0.001 mV/V and 0.10 ± 0.051 mV/V for left and right WBs, respectively) than the full-metal stripes. Therefore, regardless of the slight deviations of the fabricated WB geometries from an ideal cuboid shape, reliable output signals still can be expected in all cases.

4 Sensor Characterizations

4.1 *Sensor Static Response*

Following the optical and electrical characterizations of the WB, sensors were then further tested in force-loading

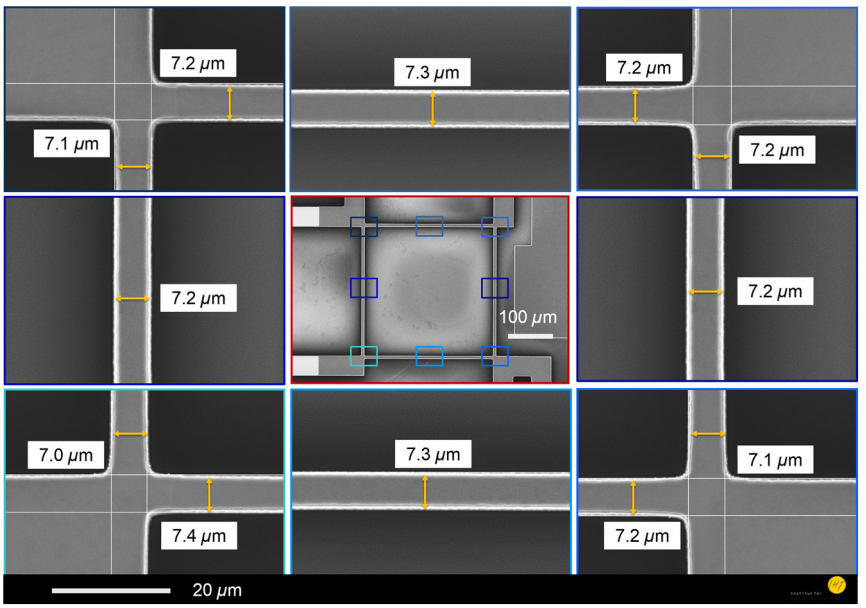

Fig. 9 SEM images of the fabricated etched *p*-SOI WB with its magnified views on its middle and corner parts for quality inspection from optical measurements.

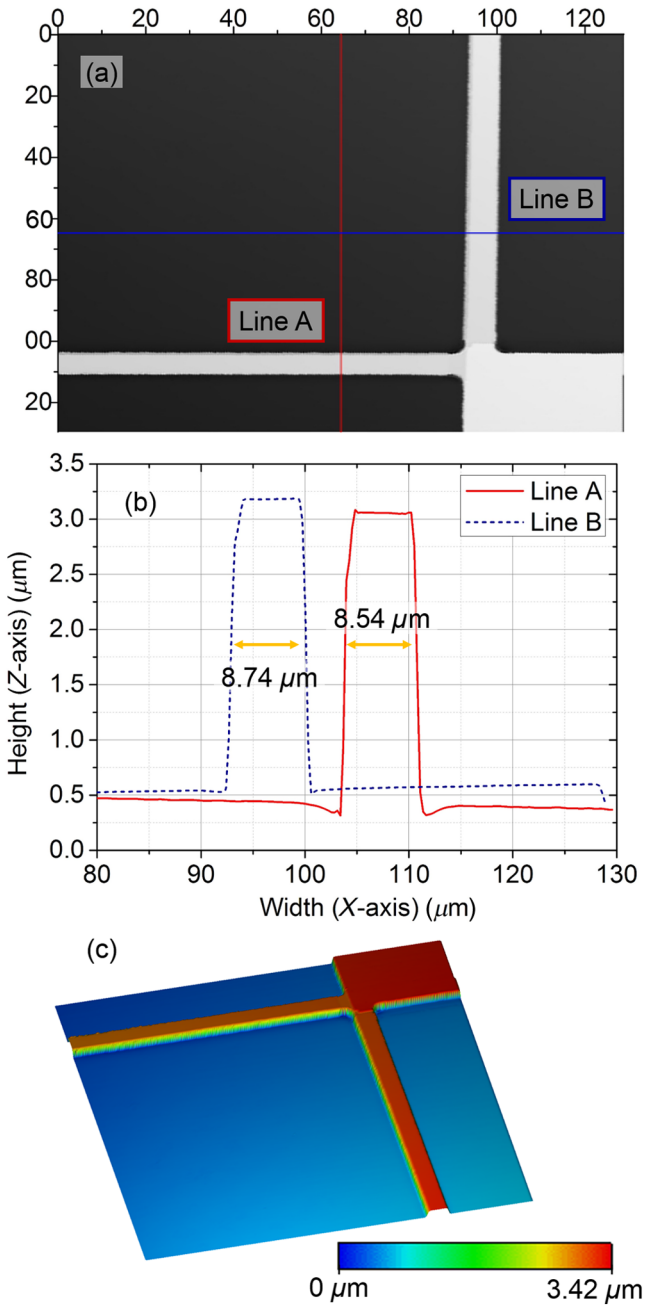

Fig. 10 (a) One corner of the etched WB under test in 3-D laser microscope showing two cross section lines (i.e., lines A and B) to characterize (b) the width and (c) the height of the piezoresistor structures.

measurements for investigating its mechanical properties and to confirm the benefits of the engineered meander springs, as it would be used as a microforce calibration standard. Moreover, to guarantee constant temperature, humidity, and pressure during the measurement as well as to eliminate measurement errors caused by environmental issues, the sample was placed inside a controlled chamber imitating normal laboratory conditions ($T = 24 \pm 0.02$°C, $rH = 37\%$). Figures 12(a) and 12(b) show the device under test, where the silicon microforce sensor was fixed on an aluminum block holder, which could be moved in 3-axis directions. Precise positioning of this part was secured by a nanopositioner with a resolution of 1 nm and a maximum

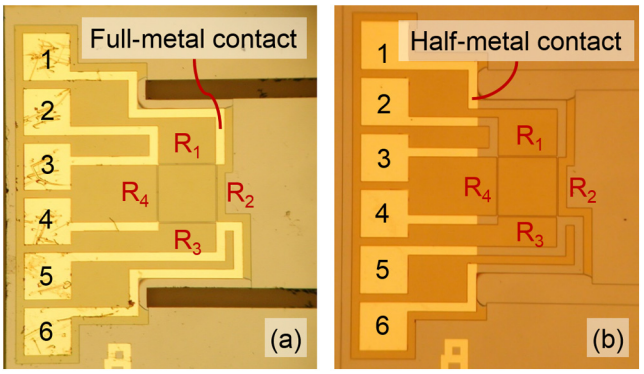

Fig. 11 Optical micrographs of the piezoresistive etched WBs with (a) full- and (b) half-metal contacts.

displacement of 100 μm.[23] The applied forces were measured by a compensation balance through a ruby sphere with a diameter of 300 μm as the mechanical contact element. In this study, the force was limited to 70 μN to avoid overloading the structure. Meanwhile, the measured data acquisition was performed in every 400 nm steps of z-direction (i.e., parallel to the loading shaft). It is crucial to ensure linear beam behavior within the sensor operating range, because at a certain point too high applied forces may

Table 3 Electrical properties different metallization type.

Measured values	Half-metal stripes	Full-metal stripes
WB resistors (left side) (Ω)	$R_{13} = 2871$	$R_{13} = 2148$
	$R_{14} = 3875$	$R_{14} = 2861$
	$R_{16} = 3327$	$R_{16} = 2162$
	$R_{23} = 318$	$R_{23} = 4$
	$R_{34} = 2631$	$R_{34} = 2150$
	$R_{36} = 3614$	$R_{36} = 2857$
	$R_{46} = 3086$	$R_{46} = 2192$
	$R_{56} = 1344$	$R_{56} = 10$
WB resistors (right side) (Ω)	$R_{13} = 3199$	$R_{13} = 2151$
	$R_{14} = 3998$	$R_{14} = 2865$
	$R_{16} = 3899$	$R_{16} = 2165$
	$R_{23} = 218$	$R_{23} = 7$
	$R_{34} = 3378$	$R_{34} = 2153$
	$R_{36} = 4148$	$R_{36} = 2861$
	$R_{46} = 2670$	$R_{46} = 2195$
	$R_{56} = 962$	$R_{56} = 7$
WB offset (left side) (mV/V)	0.03 ± 0.001	4.82 ± 0.005
WB offset (right side) (mV/V)	0.10 ± 0.051	4.82 ± 0.001

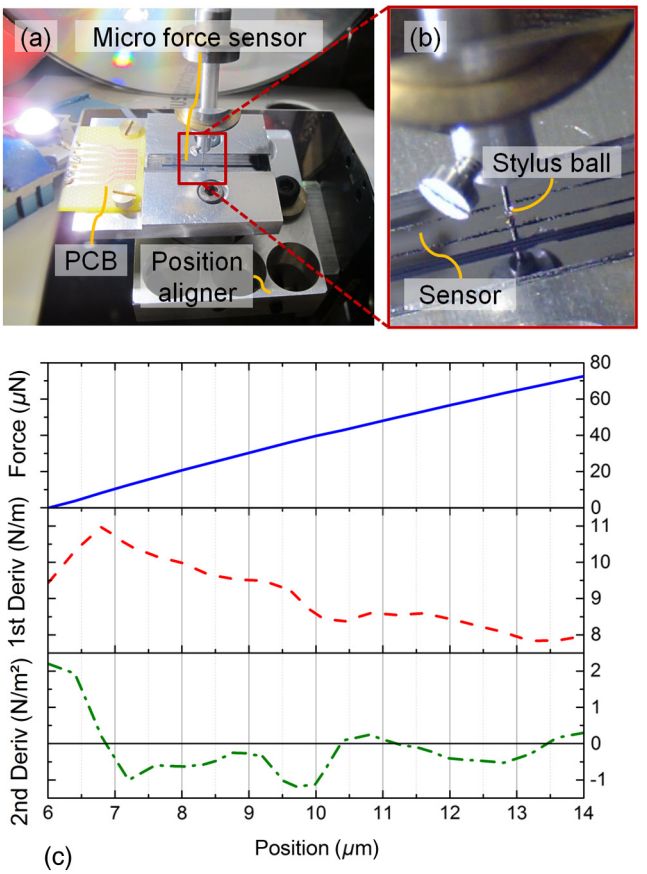

Fig. 12 Photographs of (a) the microforce sensor under test using (b) a microshaft attached with a stylus ball for applying force on the center of the boss. (c) Measurement results in the force range of 0 to 70 μN showing linear profile.

cause nonlinear force-deflection curve as well as device fracture. Figure 12(c) exhibits a typical measured position-force curve of a microforce sensor and its first and second derivatives, which exhibit very good linearity with increasing force.

The mechanical measurements were then repeated for 24 times to observe the sensor stability as well as to have quantitative measurement data. Hence, the device properties can be reliably extracted from the measured values. Moreover, to investigate its hysteresis behavior, the sensor monitoring was performed in both conditions of increasing and decreasing force loadings. The increasing loading started from the initial contact between the stylus ball and the boss, in which the shaft then further pushed the sensor toward its lower position. Similarly, the decreasing loading (i.e., unloading) was captured when the loading shaft had started to be pulled up toward its higher position. In these measurements, we determined three critical parameters, i.e., device stiffness, force sensitivity, and bending sensitivity. Figures 13(a) and 13(b) show the measured device stiffness in the force range from 1 to 70 μN during loading (i.e., 8.43 ± 0.02 N/m) and unloading (i.e., 8.61 ± 0.02 N/m) conditions, respectively. These measured stiffness values are almost three times lower than that of FEM (i.e., 23.39 N/m), which can be attributed to the overetching of the meander springs leading to a stiffness reduction [Fig. 8(c)]. Furthermore, some parts of the meander structures were not completely released, causing a reduction of the stiffness. On the other hand, the measured sensitivity values of the sensor with respect to the bending forces are 15.19 ± 0.05 V/N and 14.82 ± 0.04 V/N during loading and unloading of the shaft, respectively [Figs. 13(c) and 13(d)]. It is also interesting to determine the bending sensitivity. From Figs. 13(e) and 13(f), it is found that their measured values are in the ranges of 128.54 ± 0.19 and 128.16 ± 0.23 V/m for loading and unloading conditions, respectively. All in all, the measurement values for those three parameters of the sensor mechanical properties have exhibited very small hysteresis (<3%), confirming the performance consistency and device stability on both loading and unloading characterizations.

Additionally, the performance of the fabricated double-meander force sensors is evaluated by direct comparison of their experimental and simulation results (Table 4). For the stiffness, the final fabricated device has a lower mean value of 8.52 ± 0.02 N/m, which is almost half that of the FEM. In contrast, the mean fabricated sensor sensitivity yields higher mean value than the FEM results (i.e., 15.01 ± 0.05 V/N). Regardless of the required fabrication optimizations (e.g., improved etching process and spring designs), a combination of low stiffness and high sensitivity compared with the FEM solutions is beneficial for precise measurement procedures of very low forces.

4.2 *Sensor Dynamic Response*

In addition to the static response of the sensor, two real-time measurements (i.e., with constant and varied transverse loading speeds) were carried out to evaluate the dynamic response of the device, which is particularly exciting for robotics or automated systems based applications. In the first experiment, the signal of WB of the force sensor was monitored at the initial state, where there was no contact between the stylus and the device. Once the stylus had moved downward onto the sensor contact area and loaded the sensor with a defined velocity v_s of 5000 μm/s and a force of 305 μN, a maximum deflection Δz of 4.2 μm could be obtained. At this stage, the signal was measured within ~1 s and its average value was calculated to investigate the stability of the sensor under loading condition [Fig. 14(a)]. Afterward, the stylus was released to its initial position and reached its stable condition by experiencing an ~0.5-s oscillation [Fig. 14(b)]. The output voltage without and with contact loadings are 23.205 ± 0.092 and 24.548 ± 1.652 mV, respectively. After repeating the measurements three times, similar values of the output voltage during contact are obtained, confirming the reproducibility and reliability of the device. Furthermore, from the flexural frequency measurement, the device has a fundamental resonant frequency of 805 Hz [Fig. 14(c)].

For the second dynamic loading measurement, the sensor was tested in different loading velocities to justify its rapid responses concerning the real applications, where the forces can be applied in various speeds. However, it should be noted that the system configuration and measurement method were kept identical as those of the first measurement. From Fig. 14(d), the initial offset voltage value was 23.091 ± 0.092 mV in the condition of no contact. Under traverse speed of 50 μm/s, the output voltage in loading position was 24.340 ± 0.116 mV. Although the indentation speed during

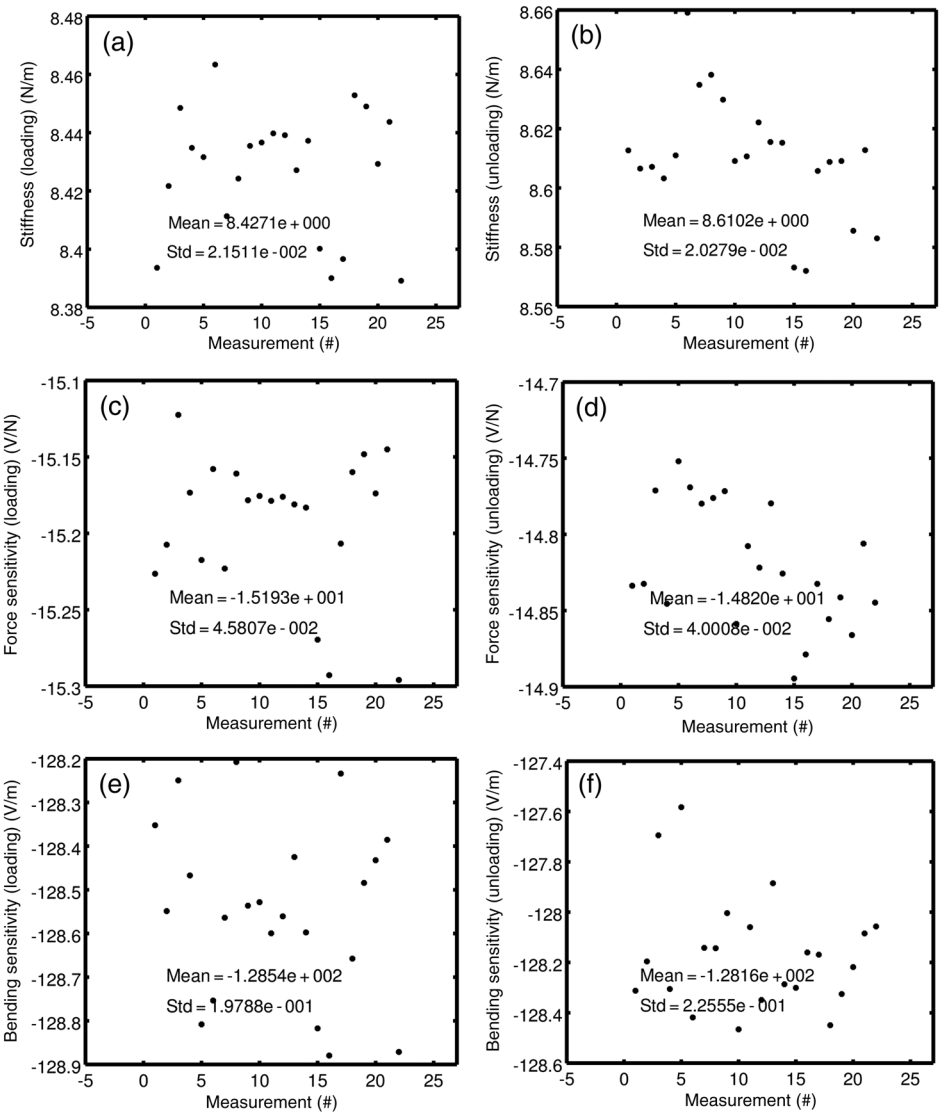

Fig. 13 Repeated measurements at one loading position on the center of the boss showing the small differences of [(a) and (b)] stiffness, [(c) and (d)] force sensitivity, and [(e) and (f)] bending sensitivity in loading and unloading conditions, respectively.

loading and unloading sequences had been increased sequentially (i.e., 500, 2500, and 5000 μm/s), the output signal of the force sensor had shown similar behavior as the one measured at the lowest speed (i.e., 50 μm/s). This could be seen from the calculated deviations of those four different output signals, which showed a very small value of <0.0008. Based on these results, the device can be considered to be potentially used to rapidly detect mechanical signal and transduce it directly into an electrical signal with stable and reliable performances.

Table 4 Comparison of device properties (numerical analysis versus fabricated device).

Device properties	Simulation results	Fabricated device (loading)	Fabricated device (unloading)
Stiffness (N/m)	23.39	8.43 ± 0.02	8.61 ± 0.02
Sensitivity (V/N)	8.07 ± 0.004	15.19 ± 0.05	14.82 ± 0.04

5 Conclusion

Piezoresistive silicon microforce sensors as a transferable calibration standard have been developed by optimizing the mechanical (i.e., springs) and electrical readout elements (i.e., piezoresistors). The meander spring design was chosen among others for fabrication because of its superior properties (i.e., lower stiffness and higher sensitivity) obtained using FEM. A particular wafer of DL-SOI has been used instead of a bulk silicon wafer to ensure very well-defined dimensions of the boss, springs, and WBs. The experimental results showed that the fabricated sensors have very good stability and properties in repeated mechanical force measurements, although their values are slightly different from those predicted by FEM. Regardless of the shown promising

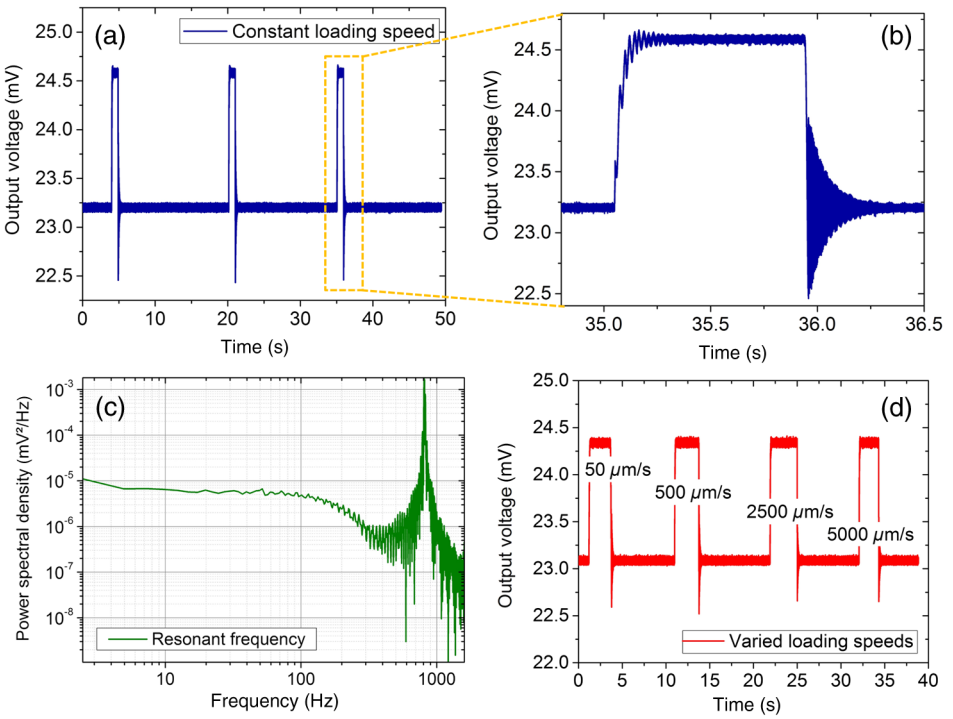

Fig. 14 Repeated dynamic measurements of microforce sensor to determine at [(a) and (b)] constant loading speed, (c) fundamental resonance, and (d) sequentially increasing loading velocity.

performance, some further experiments and optimizations are required to better justify the sensor functionality and obtain higher linearity and sensitivity.

Acknowledgments

The authors thank Juliane Arens and Doris Rümmler for their technical support. The first author gratefully acknowledges support by Braunschweig International Graduate School of Metrology (B-IGSM). This work was performed in the collaborative project "HmtS" funded by the German Federal Ministry of Education and Research (BMBF) under No. 03V0307.

References

1. M. Mehrtash et al., "Bilateral magnetic micromanipulation using off-board force sensor," *IEEE/ASME Trans. Mechatron.* **20**(6), 3223–3231 (2015).
2. L. Viry et al., "Flexible three-axial force sensor for soft and highly sensitive artificial touch," *Adv. Mater.* **26**(17), 2659–2664 (2014).
3. S. S. Kumar and B. D. Pant, "Effect of piezoresistor configuration on output characteristics of piezoresistive pressure sensor: an experimental study," *Microsyst. Technol.* **22**(4), 709–719 (2015).
4. B. Komati et al., "Prototyping of a highly performant and integrated piezoresistive force sensor for microscale applications," *J. Micromech. Microeng.* **24**(3), 035018 (2014).
5. A. M. Díez-Pascual et al., "Nanoindentation in polymer nanocomposites," *Prog. Mater. Sci.* **67**, 1–94 (2015).
6. M. C. Yip, S. G. Yuen, and R. D. Howe, "A robust uniaxial force sensor for minimally invasive surgery," *IEEE Trans. Biomed. Eng.* **57**(5), 1008–1011 (2010).
7. B. Han et al., "Silicon nanowire-based ring-shaped tri-axial force sensor for smart integration on guidewire," *J. Micromech. Microeng.* **24**(6), 065002 (2014).
8. P. S. Girao et al., "Tactile sensors for robotic applications," *Measurement* **46**(3), 1257–1271 (2013).
9. Y. Mizutani and S. Katsura, "Disturbance compensation based on data memory for macro–micro bilateral control," in *IEEE Int. Symp. on Industrial Electronics*, IEEE (2013).
10. Y. Mizutani and S. Katsura, "Analysis, modeling, and compensation of friction for scaled bilateral control," *IEEE J. Ind. Appl.* **3**(4), 344–349 (2014).
11. A. M. Ousaid et al., "A stable and transparent microscale force feedback teleoperation system," *IEEE/ASME Trans. Mechatron.* **20**(5), 2593–2603 (2015).
12. J. Frühauf et al., "Calibration of instruments for hardness testing by use of a standard," in *Recent Advancement of Theory and Practice in Hardness Measurement, Proc. HARDMEKO*, pp. 141–145 (2007).
13. *COMSOL Multiphysics Release Notes: Version 4.3b*, COMSOL AB, Stockholm, Sweden, https://www.comsol.de/shared/downloads/4.3b/ReleaseNotes.pdf (2013).
14. H. S. Wasisto et al., "Finite element modeling and experimental proof of NEMS-based silicon pillar resonators for nanoparticle mass sensing applications," *Microsyst. Technol.* **20**(4–5), 571–584 (2014).
15. M. A. Hopcroft, W. D. Nix, and T. W. Kenny, "What is the Young's modulus of silicon?" *J. Microelectromech. Syst.* **19**(2), 229–238 (2010).
16. I. Bonev and D. Zlatanov, "Advantages of the modified Euler angles in the design and control of PKMs," in *Proc. 3rd Chemnitz Parallel*, pp. 199–216 (2002).
17. S. J. Park et al., "Piezoresistive cantilever performance—part I: analytical model for sensitivity," *J. Microelectromech. Syst.* **19**(1), 137 (2010).
18. J. C. Doll and B. L. Pruitt, "Microsystems and nanosystems," *Piezoresistor Design and Applications*, Vol. **1**, Springer, New York (2013).
19. H. S. Wasisto et al., "Handheld personal airborne nanoparticle detector based on microelectromechanical silicon resonant cantilever," *Microelectron. Eng.* **145**, 96–103 (2015).
20. H. S. Wasisto et al., "Portable cantilever-based airborne nanoparticle detector," *Sens. Actuators B* **187**, 118–127 (2013).
21. H. S. Wasisto et al., "Development of silicon microforce sensors integrated with double meander springs for standard hardness test instruments," *Proc. SPIE* **9517**, 95171X (2015).
22. S. Merzsch et al., "Silicon based sensors and functional components fabricated by ICP-RIE cryogenic dry etching," in *23rd Micromechanics Microsystems European Workshop*, pp. 3–6 (2012).
23. PI Datasheet P-721, *Nanopositioning device with digital controller*, Physik-Instrumente, Karlsruhe, Germany, http://www.physikinstrumente.com/download/PI_DataSheet_P-721_42034.pdf. (2014).

Gerry Hamdana received his BEng degree in mechanical engineering from the Esslingen University of Applied Science in 2012 and his

MSc degree in mechanical engineering specializing in mechatronic/microsystems technology from the Braunschweig University of Technology (TU Braunschweig), Germany, in 2015. Currently, he is pursuing his PhD at the Institute of Semiconductor Technology (IHT), TU Braunschweig, Germany. His research interests include semiconductor micro/nanostructuring, silicon micro/nanomachining, and micro/nanoelectromechanical systems (MEMS/NEMS).

Hutomo Suryo Wasisto received Dr-Ing degree in electrical engineering, information technology, and physics with summa cum laude honor from the TU Braunschweig, Germany, in 2014. He was a postdoctoral fellow at Georgia Institute of Technology, Atlanta, from 2015 to 2016. Currently, he is head of the Optoelectromechanical Integrated Nanosystems for Sensing (OptoSense) Group in the Laboratory for Emerging Nanometrology (LENA), Braunschweig, Germany. His main research interests include nano-opto-electro-mechanical systems (NOEMS), nanosensors, nanoelectronics, and nanometrology.

Lutz Doering received his Dr.-Ing. degree in microelectronics technology, precision instrument technology, and computer science from the Dresden University of Technology, Dresden, Germany, in 1990. He joined the Department 5.1 Nano- and Micrometrology, Physikalisch-Technische Bundesanstalt (PTB), Braunschweig, Germany, in 2001. His current research interests include characterization and optimization of micromachined cantilever sensors designed for measuring coordinate and roughness parameters and for the transfer of the micronewton and nanonewton force standard to tactile probing tools.

Chunlei Yan received his Bachelor of Science degree in integrated circuit design and integrated systems from Xidian University, China, in 2012. Currently, he is pursuing his master's degree in electrical engineering at the Braunschweig University of Technology (TU Braunschweig), Germany.

Lei Zhou received her bachelor's degree in electronic science and technology from Xidian University, China, in 2013. Currently, she is pursuing her master's degree focusing on nanosystems engineering at the Braunschweig University of Technology (TU Braunschweig), Germany.

Uwe Brand received his PhD in physics from the TU Braunschweig, Germany, in 2000. Since, 2010 he has been the head of working group 5.11 hardness and tactile probing methods in Physikalisch-Technische Bundesanstalt (PTB), Braunschweig, Germany. His main research interests include the development of the nanoindentation technique and standard devices. His research group creates the basis for the traceability of hardness measurements in industry, research institutes, and calibration laboratories.

Erwin Peiner received his PhD in metastable binary metal compounds by ion beam mixing from the University of Bonn, Bonn, Germany, in 1988, and the Venia Legendi degree in semiconductor technology from the Faculty of Mechanical and Electrical Engineering, TU Braunschweig, Braunschweig, Germany, in 2000. Currently, he is the leader and professor of the Semiconductor Sensors and Metrology Group, IHT. He is the project coordinator of the collaborative project "HmtS" funded by the BMBF.